

Effect of Inflow Boundary Conditions on Hovering Tilt-Rotor Flows

Upendar K. Kaul
NASA Ames Research Center, USA.

Hovering XV-15 tilt-rotor flow predictions corresponding to 10-degree collective pitch have been made with OVERFLOW2 using Spalart-Allmaras turbulence model with Detached Eddy Simulation Formulation (SA-DES) and SST-DES turbulence models. The SA-DES and the SST-DES models were used with various levels of free-stream turbulence. The results show that the SA-DES model produces monotonically increasing higher levels of turbulence in the laminar-turbulent region near the leading edge on the rotor blade with increasing levels of far-field Reynolds number of turbulence. Similar behavior is exhibited by the SST-DES model with increasing levels of far-field turbulence kinetic energy, but only at radial stations away from the hub. The XV-15 hovering solutions are compared with experimental sectional skin friction profiles and the Figure of Merit (FM) data. Blade boundary layer profiles and sectional pressure profiles are also shown. The results show varying degrees of agreement between the predicted and the experimental FM corresponding to different inflow turbulence levels. Predictions also show disagreement with the experimental skin friction profiles in the region near the blade leading edge since the hovering tilt-rotor experiment shows transitional flow near the blade leading edge at a unit Reynolds number of 3.514×10^5 that can only be modeled by an appropriate transition model, not considered here.

Keywords: Computational Fluid Dynamics, Turbulence Modeling, Inflow Boundary Conditions, rotorcraft hovering flows.

1 Introduction

Fully turbulent predictions¹ of Figure of Merit (FM) for the hovering XV-15 rotor flow slightly overpredict the experiment²⁻⁷ at collective pitch of 10 degrees. These simulations were carried out with the default free stream turbulence level as inflow boundary conditions (b.c.) provided in OVERFLOW2.2c. The present study primarily assesses the effect of inflow turbulence levels used with SA-DES and SST-DES models on the hovering rotor flow predictions, specifically, blade-sectional skin friction, pressure, boundary layer profiles and the rotor FM, via a comparison with the experimental skin friction and the FM data²⁻⁶.

The influence of inflow values of the transport variable, μ_t/μ_l , in the SA-DES turbulence model⁸⁻¹⁰, which is traditionally referred to as Reynolds number of turbulence, R_t , is investigated by comparing these quantities at selected radial stations. Similarly, the effect of inflow values of the turbulence kinetic energy, k_∞ , in the SST-DES model is also considered. Since the experimental investigation²⁻⁶ revealed the transitional aspects of the hovering XV-15 rotor flow near the leading edge at a unit Reynolds number of 3.157×10^5 , it is critical to note here that the near-equilibrium SA-DES and SST-DES models cannot reasonably predict such a flow near the leading edge of the tilt-rotor blade in hover. To emphasize, the SA-DES and SST-DES models used here do tend to predict, in a crude manner, the near-leading edge pre-turbulent flow on the blades. The author refrains from calling this solution behavior near the leading edge as laminar-turbulent transitional, since that is not what these near-equilibrium turbulence models are capable of doing. But, using higher levels of inflow turbulence, the effects of this predicted false transition near the blade leading edge can be minimized leading to a turbulent-like profile which can then be modulated appropriately using an intermittency function based approach^{12,13} to yield a true transition profile. However, the prediction of a true transition behavior is beyond the scope of the present study. But, the effects of far-field or inflow turbulence levels on the overall hovering rotorcraft flow field are too significant to be ignored. Hence the

present study. Since experimental data on skin friction are now available^{5,6} for the XV-15 rotor blades in hover, it has made this study possible. The goal of this study is to afford a means of improving the predictions of various quantities such as C_p , C_f and FM for rotorcraft flows. Any slight increase in FM translates to an increased payload carrying capacity of helicopters, and better prediction of these quantities leads to improved resolution of the the flow-field vorticity dynamics and hence a better understanding of processes involved that can lead to quieter rotorcraft.

Various versions of the SA model listed at the national Turbulence Model Benchmarking Working Group (TMBWG) website¹¹ offer options to select the appropriate version of the SA model for a given simulation. The XV-15 rotor flow simulation study carried out in Ref. 1 used the version of the SA model referred to as SA-fv3¹¹ with the f_{t2} term set to zero. The choice of the SA-fv3 model over the standard SA model was made to prevent source terms from becoming negative¹¹ and the f_{t2} term in the standard SA model was devised to delay flow transition so that a trip term (f_{t1} term) could be used meaningfully. With this version of the SA model, prediction of the transition-like behavior of various profiles would mislead researchers into interpreting this as a true transitional behavior. As shown below, only higher values of turbulence imposed at the inflow boundaries would ensure the realization of a more developed turbulent or at least a turbulent-like profile. In that sense, the SA-fv3 model can be compared to a very quiet wind-tunnel where with quiet inflow boundary conditions, transitional behavior is likely at a given Reynolds number. On the other hand, e.g., the SA-Ia model¹¹ which has trip terms incorporated in it, can be compared to a wind-tunnel with a trip somewhere upstream which guarantees a fully developed turbulent flow with little sensitivity to the turbulence levels imposed at the inflow boundary. Therefore, the choice of the SA model used here is not entirely arbitrary. The effect of the inflow boundary conditions imposed can also be realized by a proper selection of source terms in the turbulence solving governing equations. However, since the SA-fv3 model has been widely used in OVERFLOW2 for the rotary wing flow predictions, predictions reported in high-lift and drag-prediction workshops as well as other applications, it is useful to assess the effect of inflow boundary conditions using this model for these flows.

2 Problem Statement

It is shown in internal flow simulations^{14–16} as well as in external flow simulations¹⁷ that inflow or far-field boundary conditions are too important to be ignored. Unless a given turbulent flow is in equilibrium or has attained a state of self-preservation, the choice of inflow turbulence levels has a strong bearing on the simulated turbulent flow. To the author’s knowledge, this issue was first quantified in the Space Shuttle Main Engine (SSME) Turn-Around Duct (TAD) study¹⁶.

Therefore, the higher the values of $R_{t\infty}$ or k_∞ used in the far field or at the inflow boundary, the more the likelihood of precluding laminar and laminar-turbulent transition on the blade. Similar argument holds for the reference Reynolds number. There are other factors too such as surface roughness, imposed pressure gradient in internal flows, angle of attack in external flows, geometrical shape parameters, Mach number effects, etc. that have an influence on the downstream development of turbulence^{14–17}, but these factors are not considered here.

The level of free stream turbulence to be imposed as inflow boundary condition depends on how far the computational boundary is from the body in flight, the reference Reynolds number, the turbulence model itself, etc. So there is no hard and fast rule for the inflow b.c. prescription. For the rotary wing flow simulation, the present study will throw some light in this regard.

In the present study, hovering XV-15 rotor flow at collective pitch angle of 10 degrees, unit $Re = 3.514 \times 10^5$ and $M_{tip} = 0.69$, was simulated with the SA-fv3-DES model, hereafter called SA model, without the f_{t2} term¹¹. Various values of R_t were chosen corresponding to increasing levels of inflow turbulence. The off-body regions were treated as fully viscous and full turbulence model (without zeroing out any source terms) was used in these off-body regions. Corresponding simulations were also carried out with the SST-DES model, hereafter called the SST model, by increasing the inflow turbulence kinetic energy, k_∞ , level.

3 Results

Fully turbulent XV-15 helicopter hover calculations were carried out for the following flow conditions corresponding to the experimental investigation²⁻⁶. The hover test conditions are given in Table 1.

Table 1: Salient XV-15 test conditions

Collective Pitch	Ω	C_T	M_{tip}	Re_{tip}	$UnitRe$
10 deg.	587 rpm	0.0093	0.69	4.92E+06	3.514E+05

The rotor system geometry is shown in Fig. 1(a,b). Fig. 1(b) shows a representative blade cross-sectional grid distribution where the near-tip region is indicated in green, the mid-span section in yellow and the near-hub region in blue. It is noted here that the geometry for the hub is an approximation of the actual XV-15 rotor hub.

The blade grids used are of the O-grid topology with caps at the tip and the root. The total number of grid points used for the near-body and off-body regions is approximately 45 million. The blade grid resolution for this grid is 347x212x77; 347 grid points around the blade airfoil cross-section, 212 grid points in the radial direction and 77 grid points in the blade-normal direction. The leading edge clustering is based on the tip-chord size. All the results except the FM results are discussed with respect to a given blade in hover.

Velocity profiles at selected chord-wise stations are computed to demonstrate the region of reversed flow on the blade. The velocity profiles at a given radial station are projected onto a plane normal to the radial direction to examine whether there are regions of reversed flow on the blade. This also aids in directly correlating the experimental skin friction data on the blade with the predicted velocity profiles. This procedure used for calculating velocity profiles in a general 3-D reversed flow has proved to be valuable in identifying reversed flow regions on the rotor blade.

Results are discussed in terms of various following quantities.

- Figure of Merit (FM)
- Sectional skin friction coefficient
- Sectional pressure coefficient
- Sectional velocity profiles

The effect of increasing inflow turbulence levels was assessed through Figure of Merit (FM), sectional pressure, skin friction profiles and velocity profiles at selected radial stations. Thus the effect on skin friction was also correlated to the tangential velocity profiles at various chordwise locations at $r/R = 0.28$, where reversed flow was observed experimentally.

Before discussing the computational results, a comparison with experiment should be made with the following caveat in mind. The experiments²⁻⁶ were conducted in the National Full Scale Aerodynamics Complex (NFAC), 80- by 120- ft Wind Tunnel, but the simulations were carried out in free space. Therefore, the effect of recirculation zones and the resulting induced unsteadiness observed in the experiments gives rise to a wider experimental scatter. This effect is absent in the simulation. Additionally, the computations were made with an approximate rotor hub model and with no model support system (see Fig. 2).

Also, in comparing the FM predictions with experiment, it is worth noting that in the experiment^{5,6}, 64 revs of data were acquired per data point and data points were acquired about once per minute for 15-20 minutes per test condition. Each experimental mean value was obtained by averaging over 64 revs. Many mean values were obtained corresponding to many test points and the experimental scatter is defined over these test points. The experimental scatter is necessarily wider because of the unsteadiness induced by the recirculation zones as mentioned above.

The FM predictions corresponding to the SA and SST models are shown in Figs. 3 and 4, respectively, showing the effect of the inflow turbulence level on FM. As shown in Figs. 3(a) and 4(a), FM time history runs up to a time corresponding to 16 revolutions. Figs. 3(b) and 4(b) show enlarged view of the corresponding

FM time history around the last few revolutions. It is shown that FM has reached a near-stationary cyclic state (steady periodic state). Agreement with experiment^{5,6} is good in terms of the mean value of FM, as shown in Figs. 3(b) and 4(b), although the predictions overshoot the experimental spread somewhat. The mean of the predicted FM for higher values of turbulence levels tends to agree with the experiment better than that at lower turbulence levels. Fig. 3(b) shows a monotonic trend in the FM prediction corresponding to the SA model, i.e., as $R_{t\infty}$ increases from a value of 0.0001 to 10,000.0, FM decreases correspondingly from a mean value of 0.776 to 0.773. Similarly, with the SST model, as k_∞ increases from 1E-06 to 1E-01, FM decreases from 0.772 to 0.766. This is in keeping with the physical argument that as the turbulence level on the rotor blade increases, FM will decrease since the torque coefficient will also correspondingly increase, with little change in the thrust coefficient.

Figs. 5(a-f) and 6(a-f) show predicted sectional pressure profiles at various radial stations corresponding to 6 different values of $R_{t\infty}$ with the SA model. As the inflow turbulence is increased from a value of $R_t = 0.0001$ to 10000.0, the pressure profiles show a slight change.

Figs. 7(a-f) and 8(a-f) show predicted sectional pressure profiles with the SST model at various radial stations. The change in pressure coefficient, as k_∞ increases, is discernible just as in the case of the SA model. But, the change in the pressure profiles is significantly smaller than that in the skin friction profiles as we will see below, which suggests that the change in FM observed in Figs. 3 and 4 is mainly due to the viscous effects.

Skin friction results with the SA model at various radial stations shown in Figs. 9(a-f) and 10(a-f) correspond to 6 different values of $R_{t\infty}$. As $R_{t\infty}$ increases, skin friction in the laminar-turbulent transition region near the leading edge increases monotonically. At the radial station, $r/R=0.5$, the leading edge laminar separation bubble, as observed in the experiment^{5,6}, is not predicted in the present calculations, as shown in Fig. 9(e). Even the fully laminar calculation¹ did not predict it, suggesting that the chord-wise grid may not be fine enough in this region. However, the overall trend here is that as free stream turbulence intensity level is decreased, the skin friction profile tends to mimic the transition region though only feebly. Coles¹⁸ and Dhawan Narasimha¹⁹ observed in their experiments on a flat plate an overshoot in the skin friction profile toward the end of the transition region. Similar trend is observed in the experiment^{5,6} on the tilt-rotor blade. The experimental skin friction profile eventually asymptotes to the turbulent profile corresponding to the turbulent flow that is assumed to have originated at the leading edge of the blade. Therefore, it is the turbulent profile whose origin is the transition onset location that should be used for the intermittency function modulation in the prediction of transition region, and not the turbulent profile whose origin is the leading edge of the blade.

Figs. 11(a-f) and 12(a-f) show the sectional skin friction profiles at various stations corresponding to the SST model. As k_∞ increases, there is no overall monotonic trend in the increase or decrease of skin friction, but there is an appreciable change in the skin friction in the laminar-turbulent transition region. The SST skin friction results show a trend similar to that of the SA skin friction results, only at radial stations away from the rotor hub.

In the experiment⁵⁻⁶, a reversed flow region was observed at the radial station of $r/R = 0.28$ around the chordwise station, $x_u/c = 0.7$. This is confirmed by the computations with both the turbulence models. Figs. 13(a-f) and 14(a-f) show boundary layer profiles at three radial stations, $r/R = 0.28, 0.50$ and 0.72 . Figs. 13(a-f) show the results with the SA model. In Figs. 13(a-b), the tangential velocity profile shows a reversed flow region at $r/R=0.28, x_u/c=0.8$. Also, slight differences are shown to exist in the boundary layer profiles corresponding to 6 different values of $R_{t\infty}$. The boundary layer profiles obtained with the SST model corresponding to 4 different values of k_∞ are shown in Figs. 14(a-f). Again, the reversed flow region is shown at $r/R=0.28$ at $x_u/c=0.8$ with slight differences in the tangential velocity profiles corresponding to different values of k_∞ .

4 Conclusion and Future Work

It is reasonable to use the SA-fv3-DES model with higher values of inflow R_t to minimize transition type behavior of skin friction, etc., on the rotor blades. The dependence of the local rotor blade solution as well as the Figure of Merit on the inflow turbulence levels is shown to be discernible. Both the SA-fv3-DES and SST-DES solutions exhibit dependence on the inflow turbulence levels imposed at the far-field boundary. The

DES solutions with the SA and SST models have been obtained using the DES formulation in OVERFLOW2. These solutions have some dependence on the grid resolution away from the blades, since the grid-dependent viscosity in the DES formulation is a function of the local grid cell size. Therefore, the DES predictions are expected to show some grid cell-size dependence. Future study should investigate this dependence of the solution on the grid-dependent viscosity. The results shown here demonstrate and quantify the importance of choosing the inflow turbulence levels carefully and has led to the latest release of OVERFLOW2.2e with revised default values for inflow turbulence levels.

5 Acknowledgements

This work was funded by the Subsonic Rotary Wing Project of the NASA Fundamental Aeronautics Program. The author would like to gratefully acknowledge helpful information on the experimental results provided by Gloria Yamauchi. The XV-15 grids were provided by Jasim Ahmad and Henry Lee of NASA Ames Research Center, which is thankfully acknowledged. Review of this paper by Cetin Kiris and Jasim Ahmad of NASA Ames Research Center and by Mark Potsdam of U.S. Army is thankfully acknowledged.

6 References

¹Kaul, U. K. and Ahmad, J., "Skin Friction Predictions Over a Hovering Tilt-Rotor Blade Using OVERFLOW2," AIAA Paper 2011-3186, 29th AIAA Applied Aerodynamics Conference, June 27-30, 2009, Honolulu, Hawaii; to appear in *J. Aircraft*, 2012

²Wadcock, A. J. and Yamauchi, G. K., "Skin Friction Measurements on a Full-Scale Tilt Rotor in Hover," American Helicopter Society 54th Annual Forum, Washington D.C., May 20-22, 1998.

³Yamauchi, G. K., Wadcock, A. J. and Heineck, J. T., "Surface Flow Visualization on a Hovering Tilt Rotor Blade," American Helicopter Society Technical Specialists' Meeting for Rotorcraft Acoustics and Aerodynamics, Williamsburg, VA, October 28-30, 1997.

⁴Lau, B. H., Wadcock, A. J. and Heineck, J. T., "Wake Visualization of a Full-Scale Tilt Rotor in Hover," American Helicopter Society Technical Specialists' Meeting for Rotorcraft Acoustics and Aerodynamics, Williamsburg, VA, October 28-30, 1997.

⁵Wadcock, A. J. , Yamauchi, G. K. and Driver, D. M., "Skin Friction Measurements on a Rotor in Hover," American Helicopter Society Technical Specialists' Meeting for Rotorcraft Acoustics and Aerodynamics, Williamsburg, VA, October 28-30, 1997.

⁶Wadcock, A. J. , Yamauchi, G. K. and Driver, D. M., "Skin Friction Measurements on a Hovering Full-Scale Tilt Rotor," *J. American Helicopter Society*, Vol. 44, No. 4, pp. 312-319, October 1999.

⁷Yamauchi, G. K. and Young, L. A., Editors, "A Status of NASA Rotorcraft Research," NASA/TP-2009-215369, September 2009.

⁸Spalart, P. R. and Allmaras, S. R., "A One- Equation Turbulence Model for Aerodynamic Flows," AIAA Paper 92-0439, AIAA 30th Aerospace Sciences Meeting and Exhibit, Reno, NV, 1992.

⁹Rumsey, C. L., Allison, D. O., Biedron, R. T., Buning, P.G., Gainer, T. G., Morrison, J. H., Rivers, S. M., Mysko, S. J., and Witkowski, D. P., "CFD Sensitivity Analysis of a Modern Civil Transport Near Buffet-Onset Conditions," NASA/TM-2001-211263, December 2001.

¹⁰Spalart, P. R., "Trends in Turbulence Treatments," AIAA 2000-2306, June 2000.

¹¹<http://turbmodels.larc.nasa.gov>", Turbulence Modeling Resource, Langley Research Center

¹²Kaul, U. K., "Laminar-Turbulent Transition Calculations of Heat Transfer at Hypersonic Mach Numbers Over Sharp Cones," Collected Papers in Heat Transfer, 1988 $\text{\textcircled{D}}$ HTD, Vol. 104, Ed. K. T. Yang; Paper presented at the Annual ASME meeting in Chicago, 1988.

¹³Kaul, U. K., "Prediction of Transitional (Laminar-Turbulent) Hypersonic Flows Using the Parabolized Navier-Stokes Equations," Royal Aeronautical Society International Conference on Hypersonic Aerodynamics, September 4 $\text{\textcircled{D}}$ 6, 1989, University of Manchester, United Kingdom.

¹⁴Kaul, U. K., "Effect of Inflow Boundary Conditions on the Solution of Transport Equations for Internal Flows," AIAA Paper 2010-4743, 40th Fluid Dynamics Conference and Exhibit, June 28 - July 1, 2010, Chicago, Illinois

¹⁵Kaul, U. K., "Effect of Inflow Boundary Conditions on the Turbulence Solution in Internal Flows," AIAA J., Vol. 49, No. 2, February 2011 pp 426-432

¹⁶Kaul, U. K., "Turbulent Flow in a 180° Bend: Modeling and Computations," NASA CR-4141, Feb. 1989

¹⁷Spalart, P. R. and Rumsey, C. L., "Effective Inflow Conditions for Turbulence Models in Aerodynamic Calculations," AIAA Journal, Vol. 45, No. 10, 2007, pp. 2544-2553.

¹⁸Coles, D., Journal Aeronautical Science, Vol. 21, pp. 433, 1954

¹⁹Dhawan, S. and Narasimha, R., "Some Properties of Boundary Layer Flow During the Transition From Laminar to Turbulent Motion," J. Fluid Mech., Vol. 3, No. 4, pp. 418-436, 1958.

7 Figures

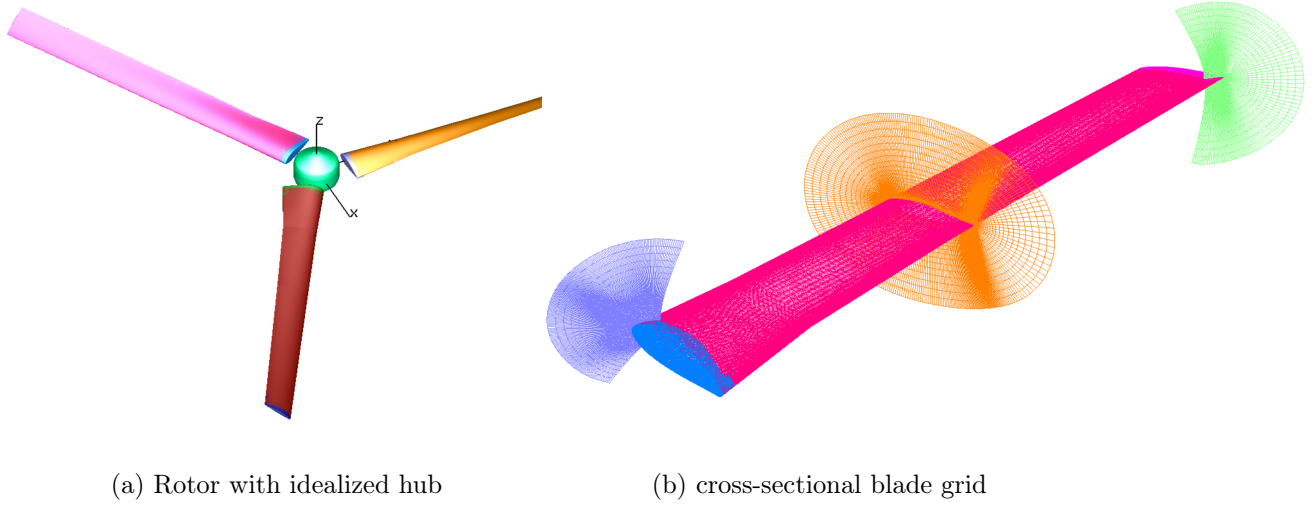
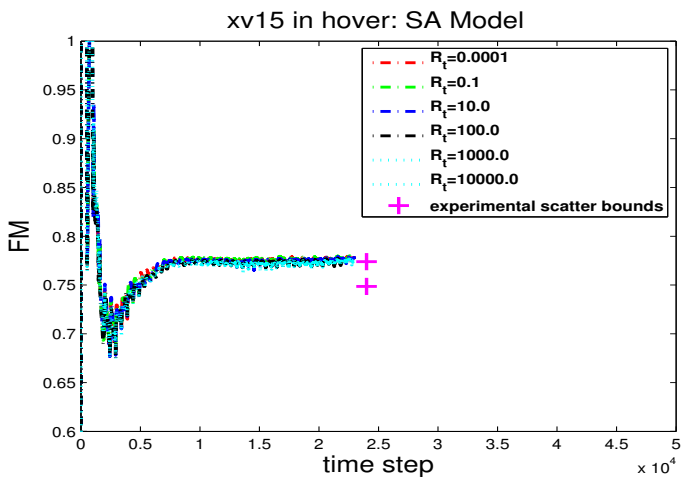


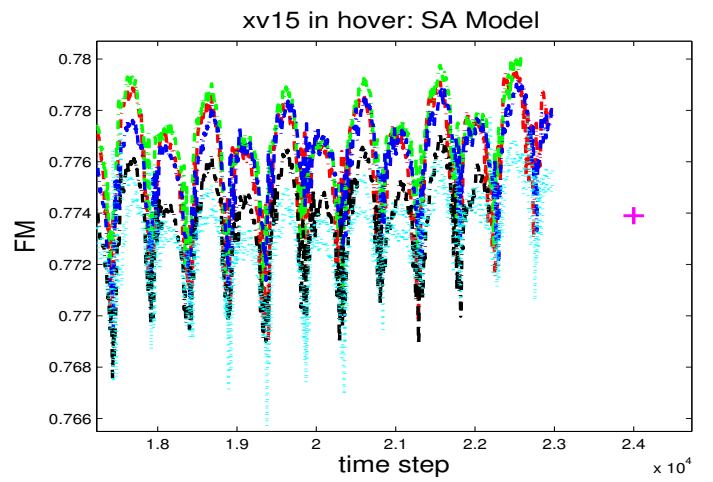
Figure 1: The XV-15 rotor geometry and blade grid



Figure 2: Experimental Set-up in the 80- by 120- ft Wind Tunnel (courtesy Wadcock and Yamauchi; Ref.6)

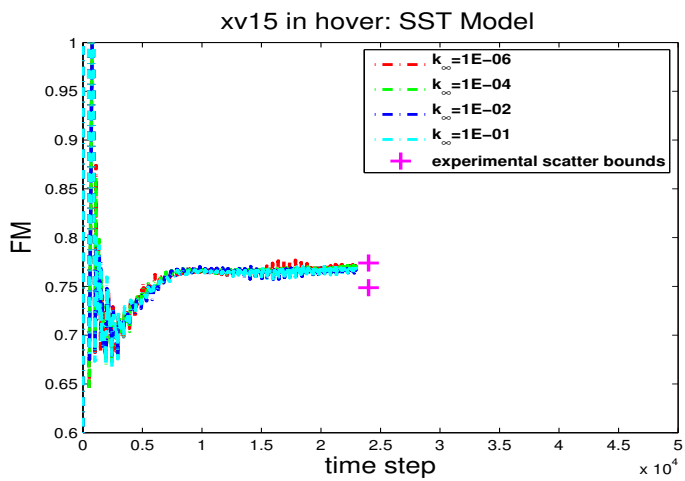


(a) 16 revolutions

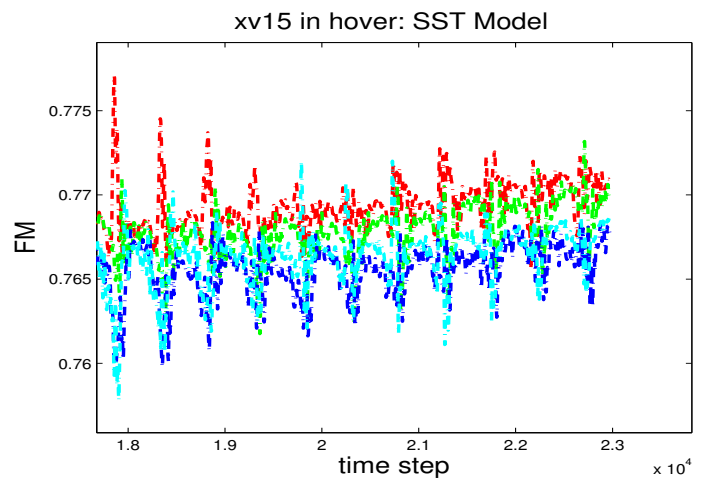


(b) 16 revolutions: enlarged view

Figure 3: SA-DES Model: Figure of Merit for 10-degree collective at tip Mach number = 0.69 (full tip speed)

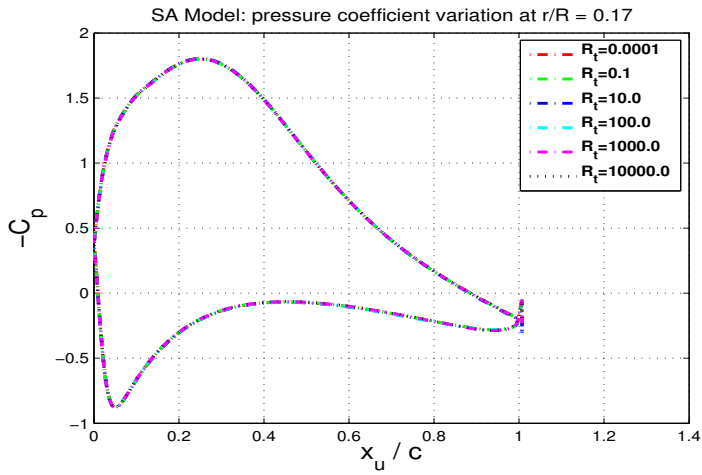


(a) 16 revolutions

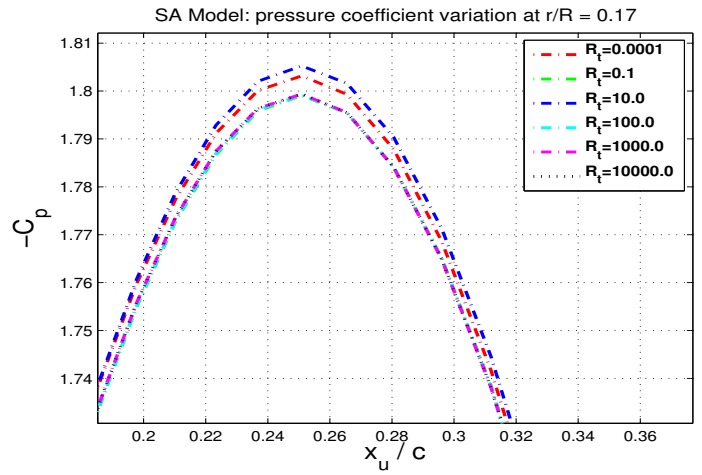


(b) 16 revolutions: enlarged view

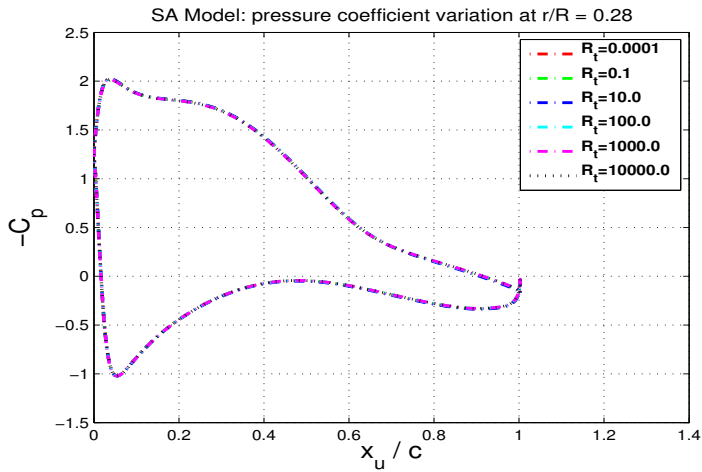
Figure 4: SST-DES Model: Figure of Merit for 10-degree collective at tip Mach number = 0.69 (full tip speed)



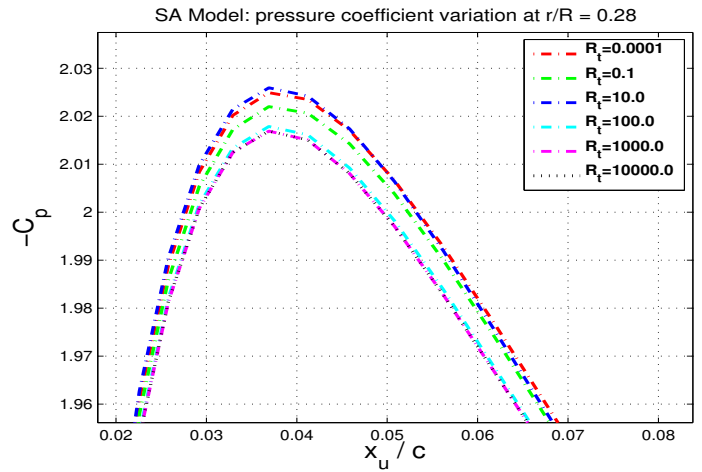
(a) $r/R = 0.17$



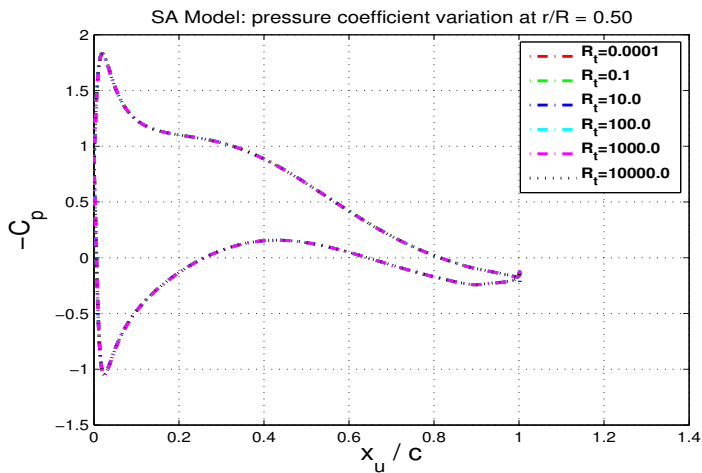
(b) enlarged view



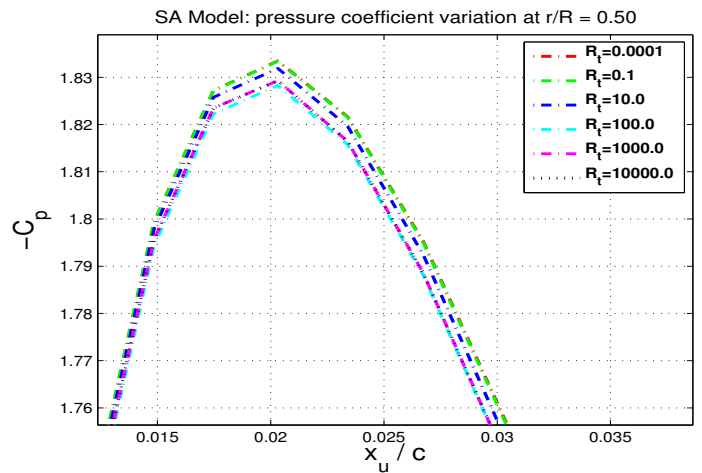
(c) $r/R = 0.28$



(d) enlarged view

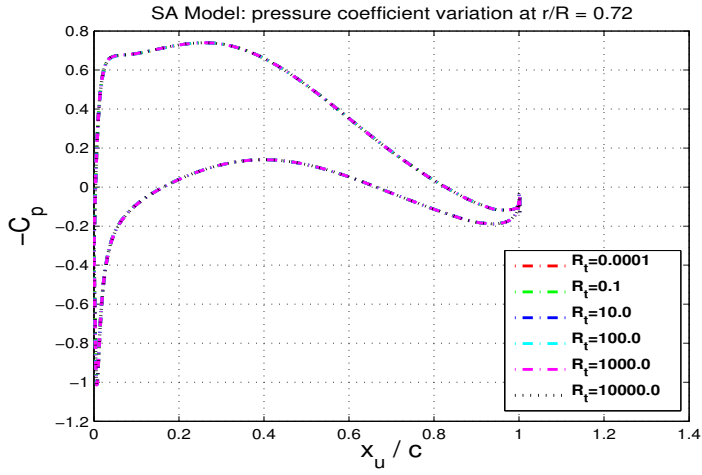


(e) $r/R = 0.50$

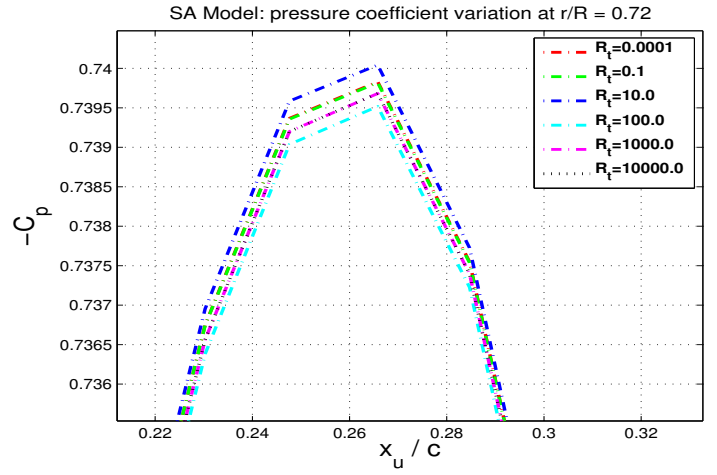


(f) enlarged view

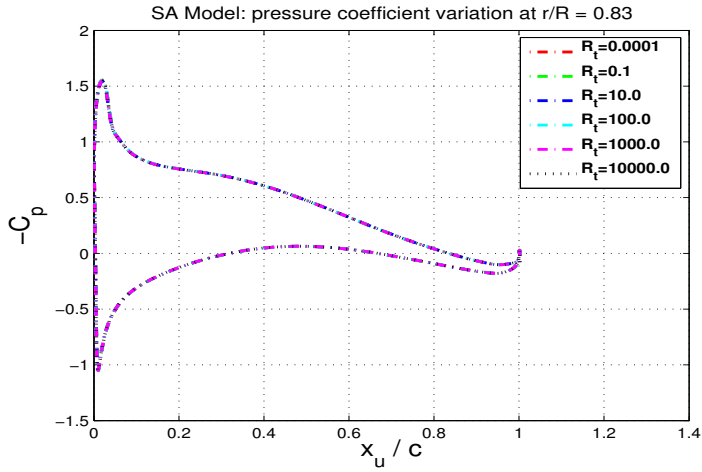
Figure 5: SA-DES Model: pressure coefficient variation along x_u (upper surface of the blade) at various radial stations corresponding to 10-degree collective pitch



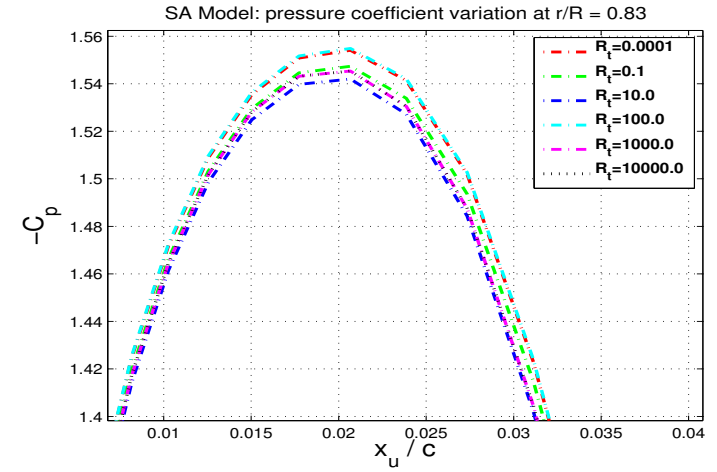
(a) $r/R = 0.72$



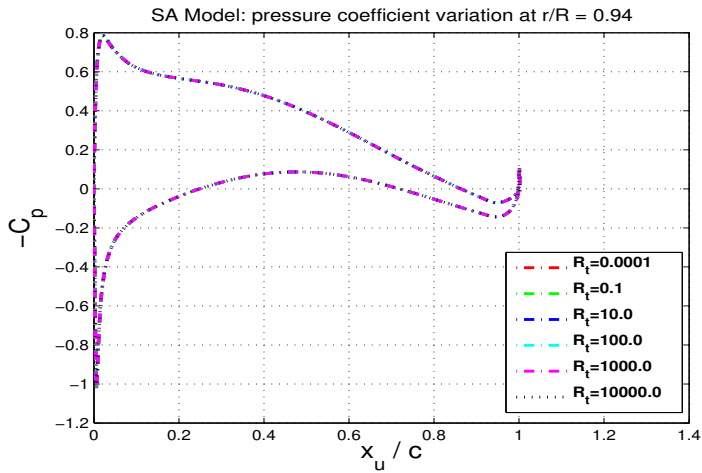
(b) enlarged view



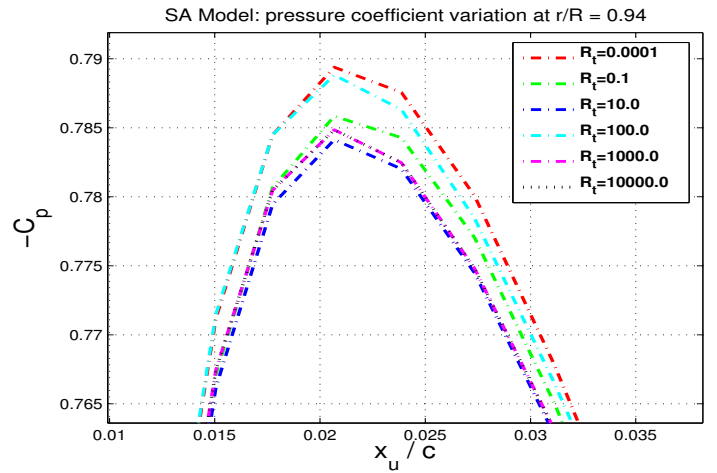
(c) $r/R = 0.83$



(d) enlarged view

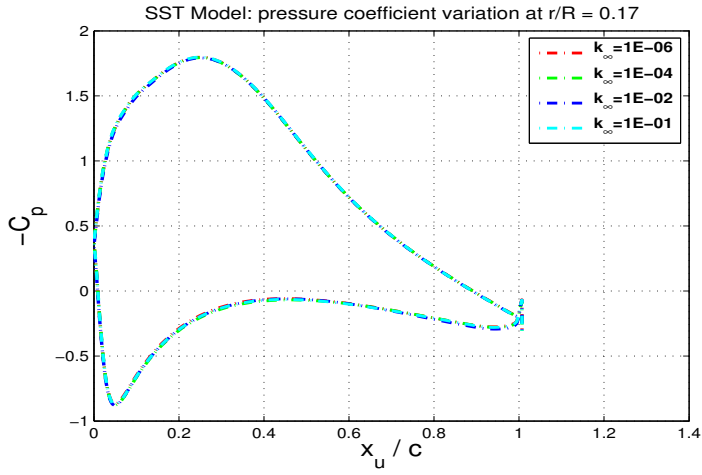


(e) $r/R = 0.94$

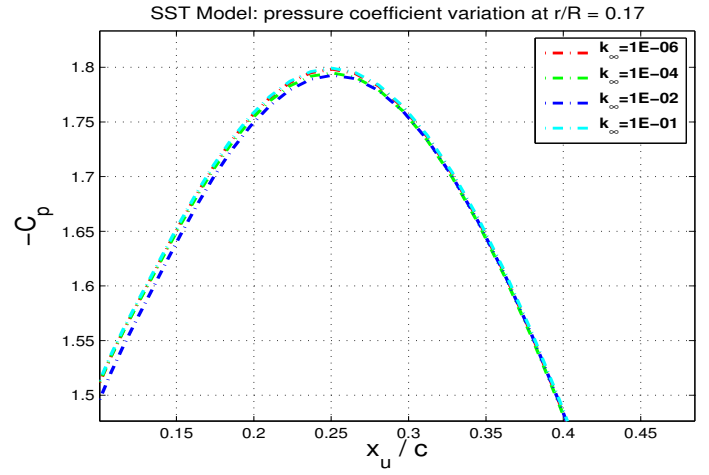


(f) enlarged view

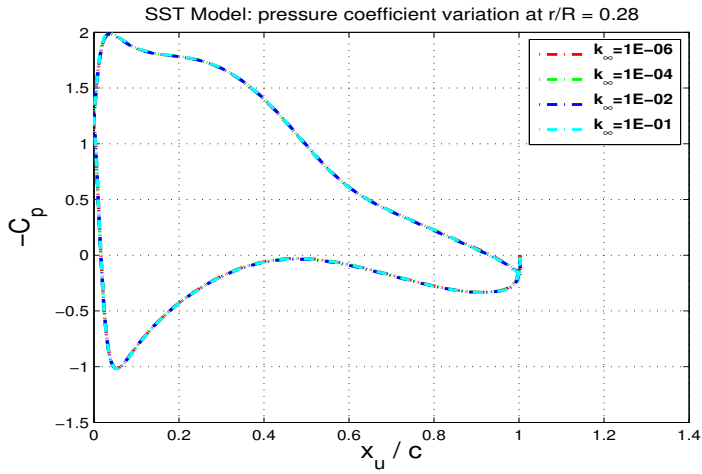
Figure 6: SA-DES Model: pressure coefficient variation along x_u (upper surface of the blade) at various radial stations corresponding to 10-degree collective pitch



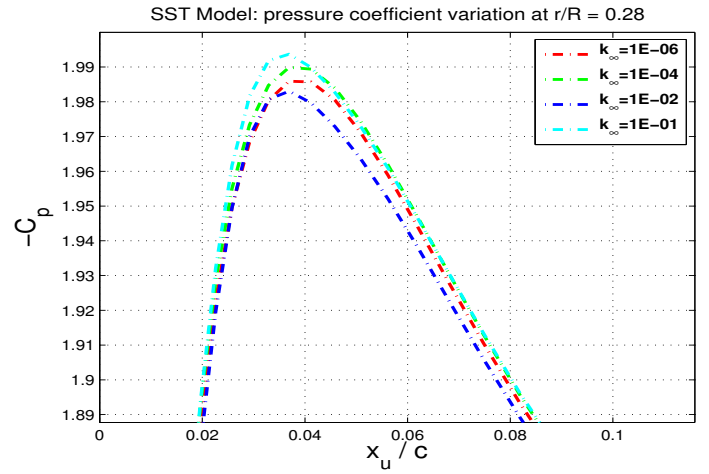
(a) $r/R = 0.17$



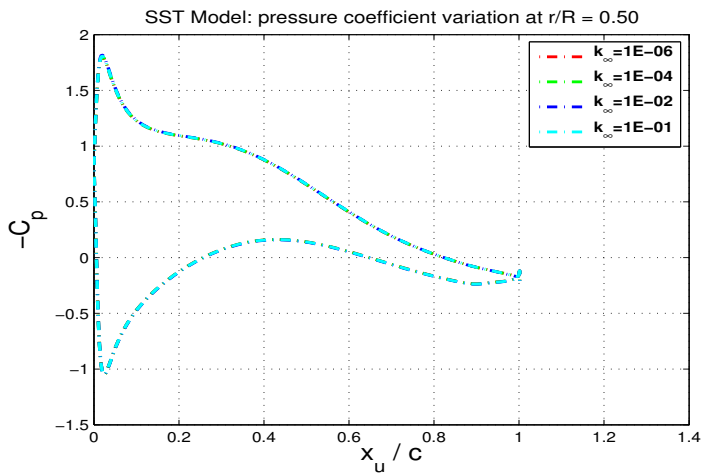
(b) enlarged view



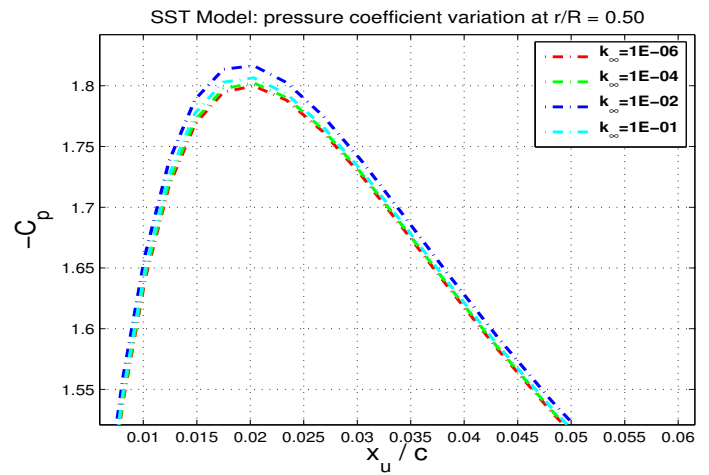
(c) $r/R = 0.28$



(d) enlarged view

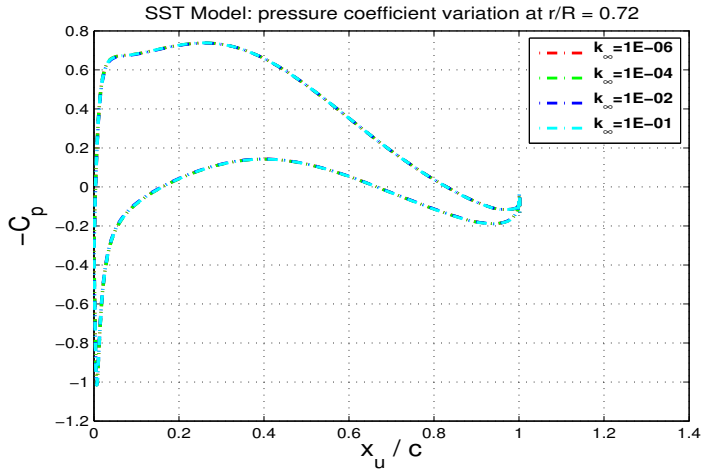


(e) $r/R = 0.50$

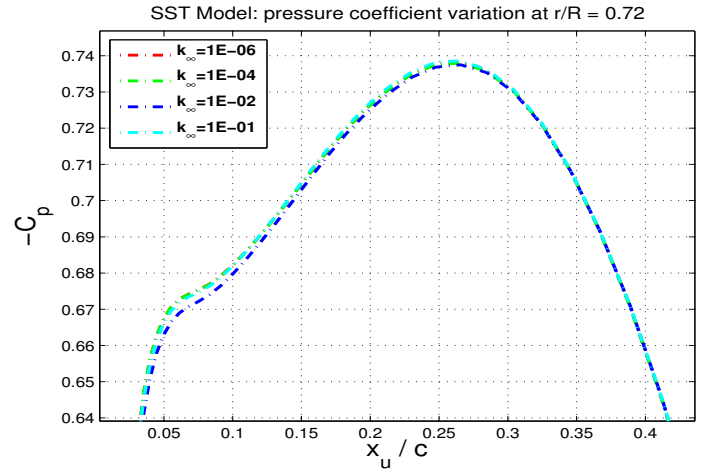


(f) enlarged view

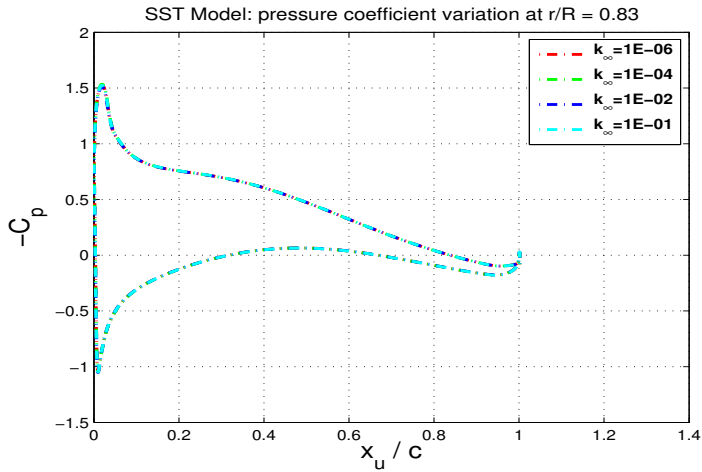
Figure 7: SST-DES Model: pressure coefficient variation along x_u (upper surface of the blade) at various radial stations corresponding to 10-degree collective pitch



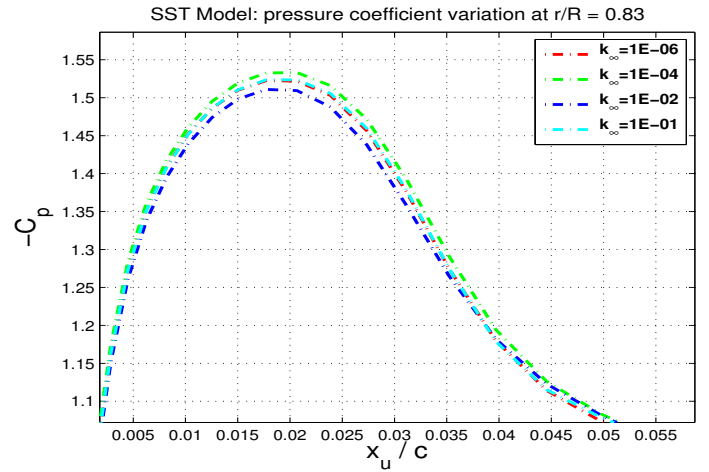
(a) $r/R = 0.72$



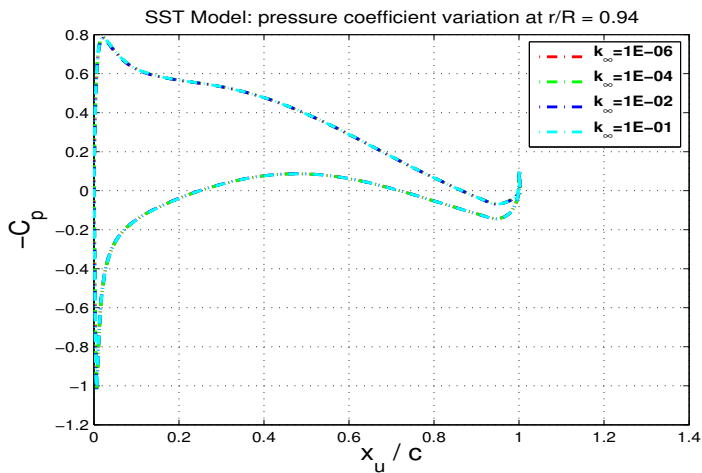
(b) enlarged view



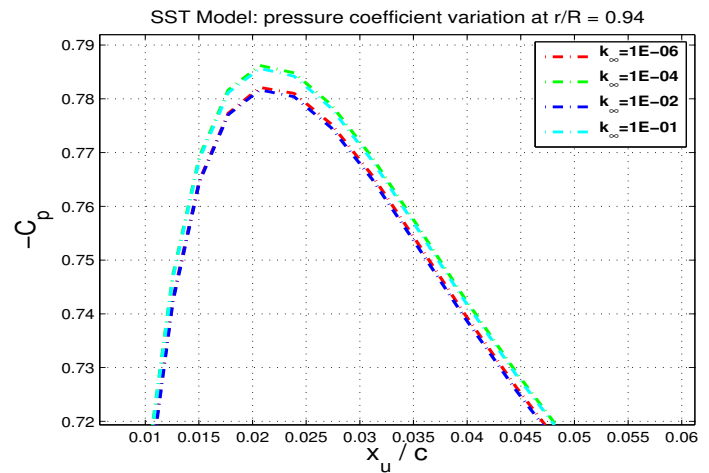
(c) $r/R = 0.83$



(d) enlarged view

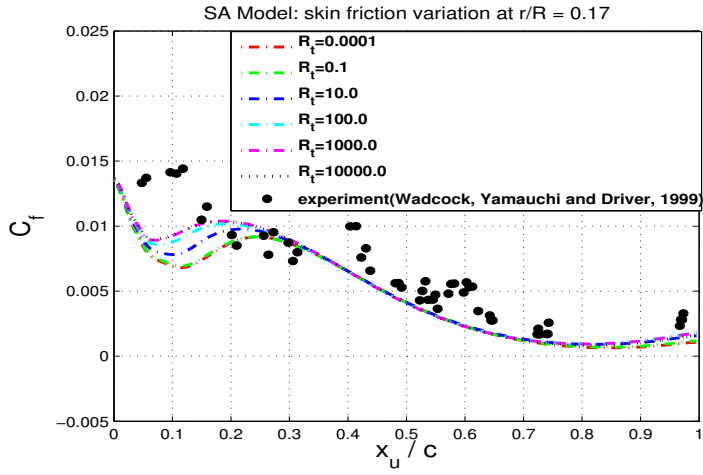


(e) $r/R = 0.94$

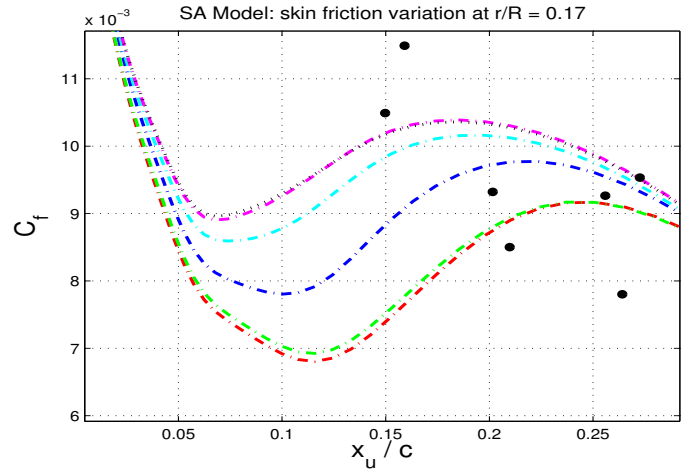


(f) enlarged view

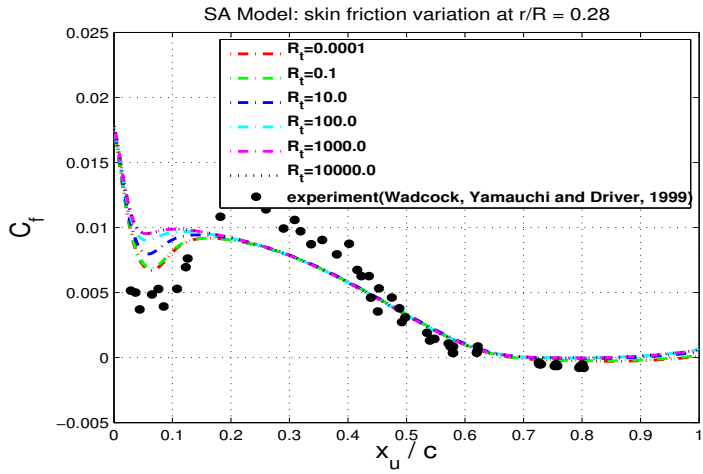
Figure 8: SST-DES Model: pressure coefficient variation along x_u (upper surface of the blade) at various radial stations corresponding to 10-degree collective pitch



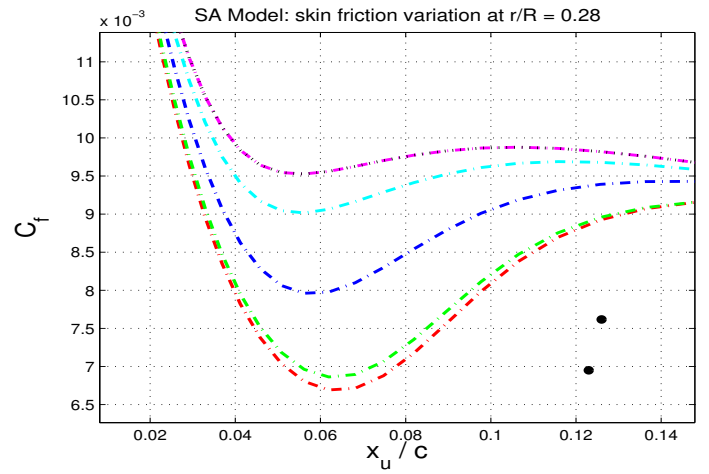
(a) $r/R = 0.17$



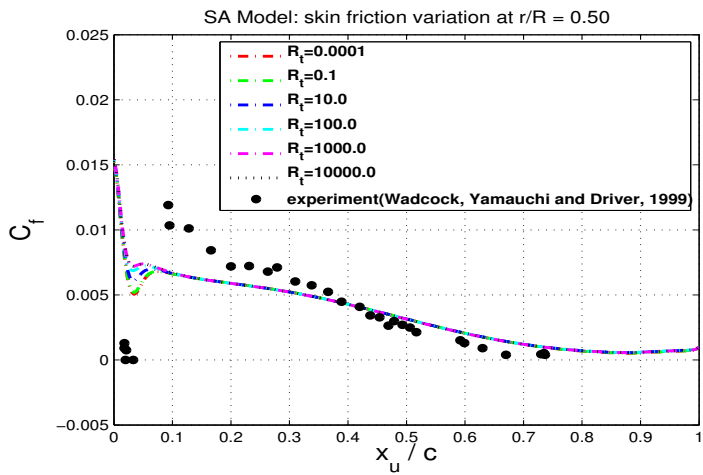
(b) enlarged view



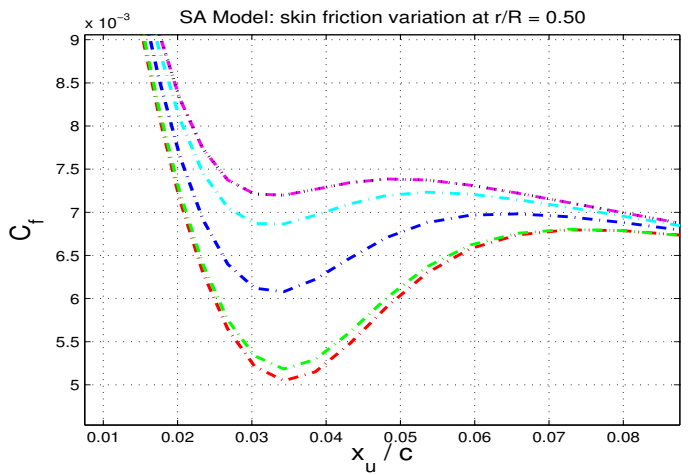
(c) $r/R = 0.28$



(d) enlarged view

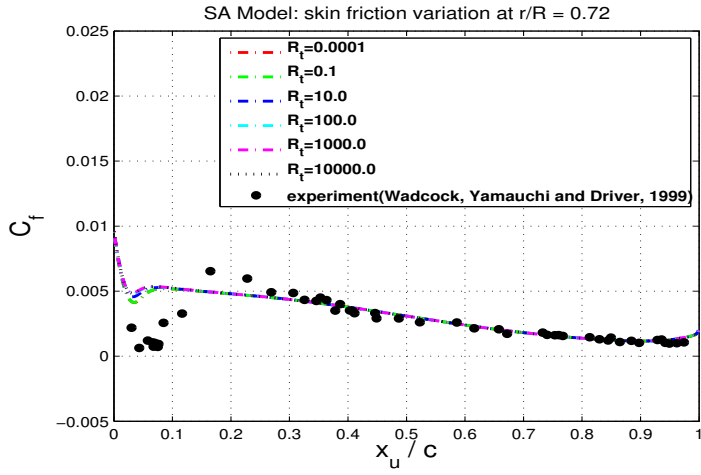


(e) $r/R = 0.50$

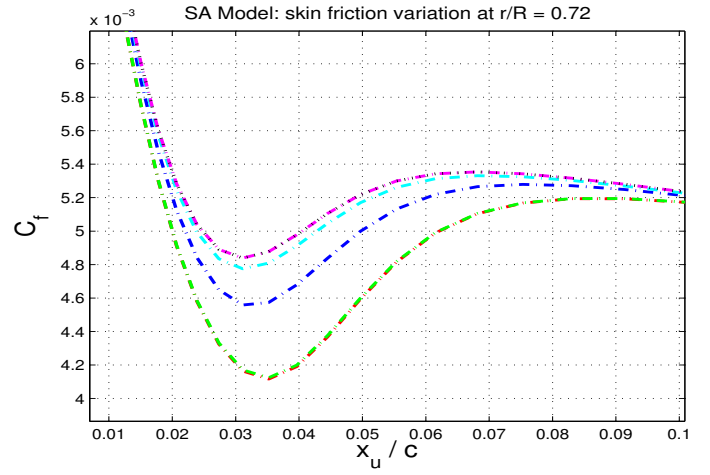


(f) enlarged view

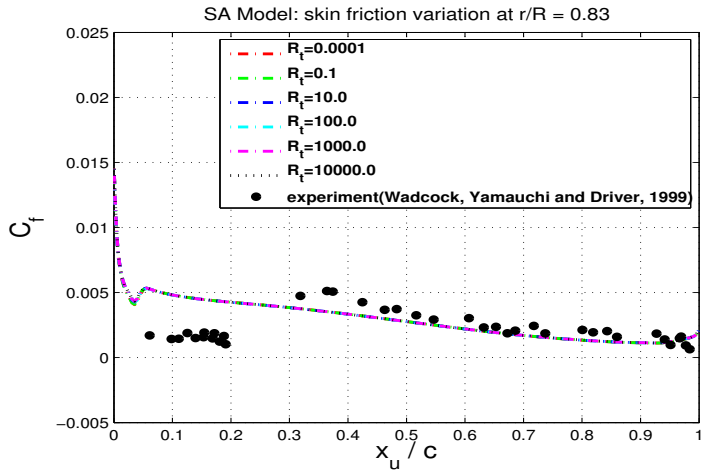
Figure 9: SA-DES Model: skin friction variation along x_u (upper surface of the blade) at various radial stations corresponding to 10-degree collective pitch



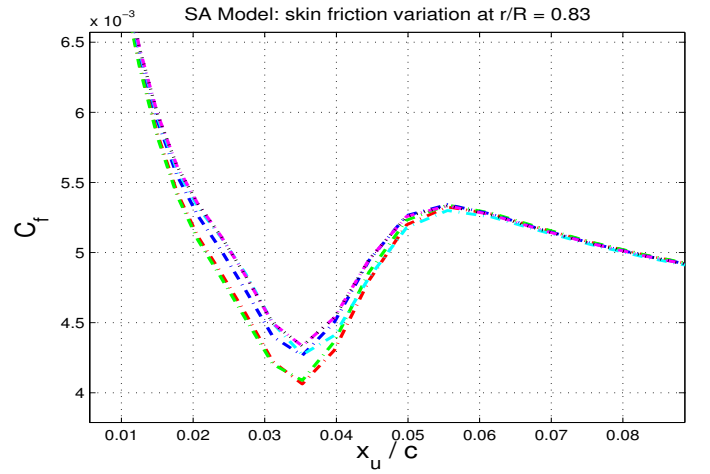
(a) $r/R = 0.72$



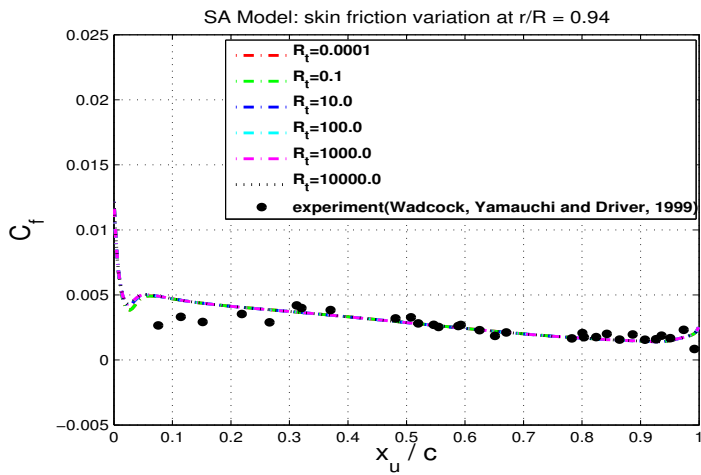
(b) enlarged view



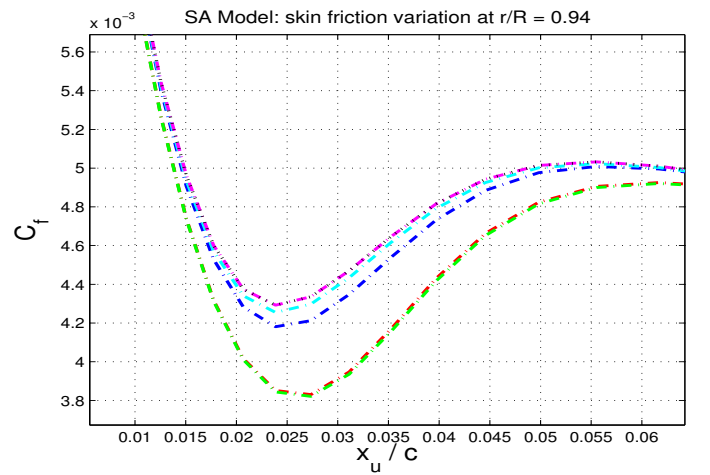
(c) $r/R = 0.83$



(d) enlarged view

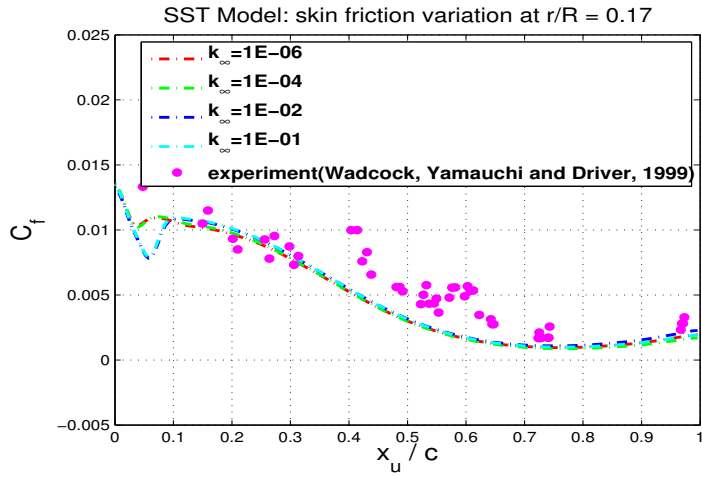


(e) $r/R = 0.94$

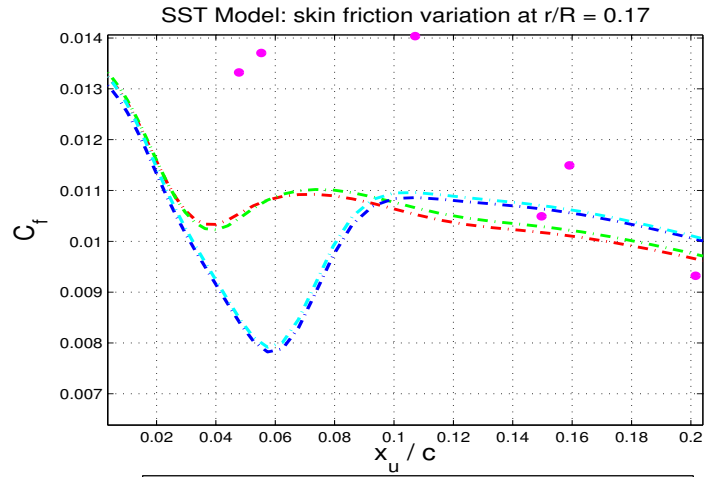


(f) enlarged view

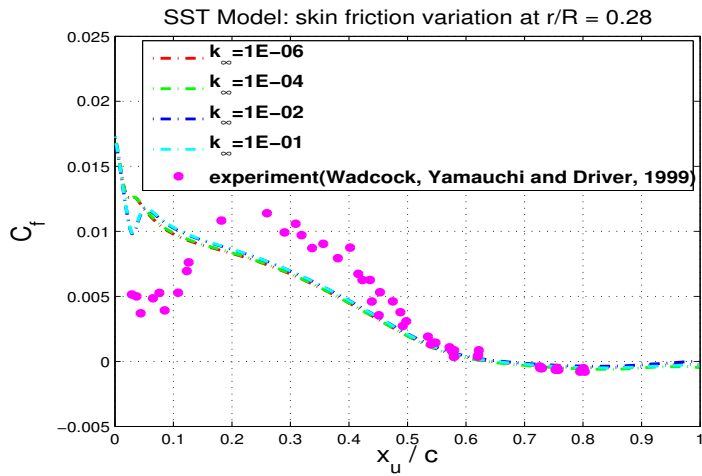
Figure 10: SA-DES Model: skin friction variation along x_u (upper surface of the blade) at various radial stations corresponding to 10-degree collective pitch



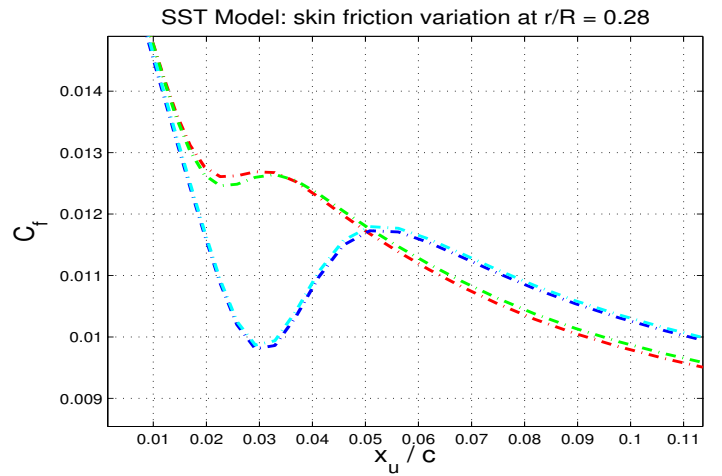
(a) $r/R = 0.17$



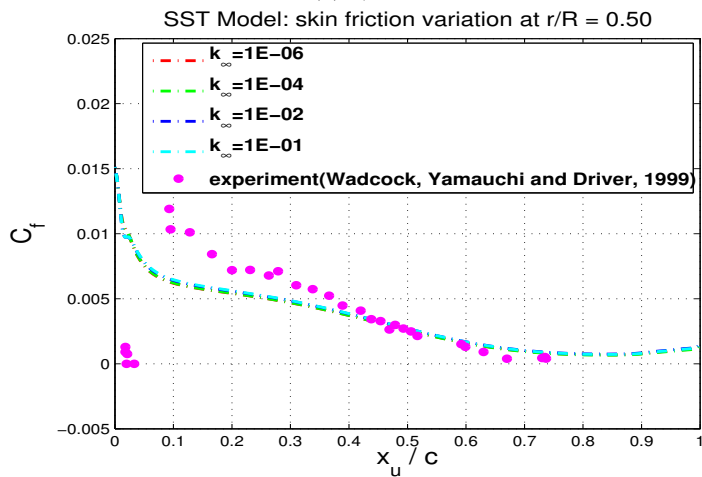
(b) enlarged view



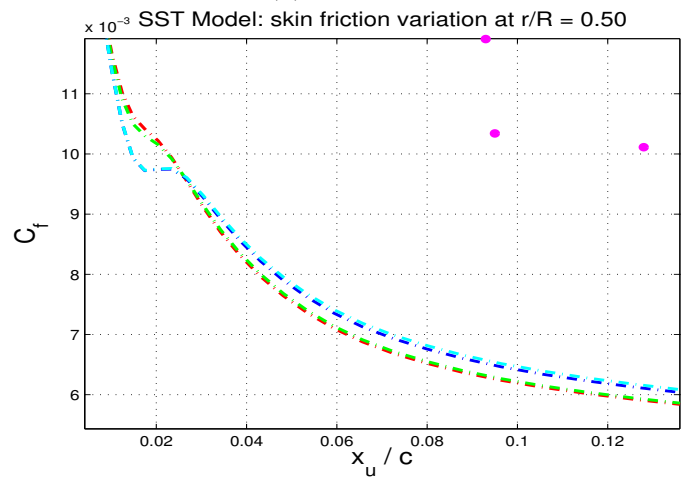
(c) $r/R = 0.28$



(d) enlarged view

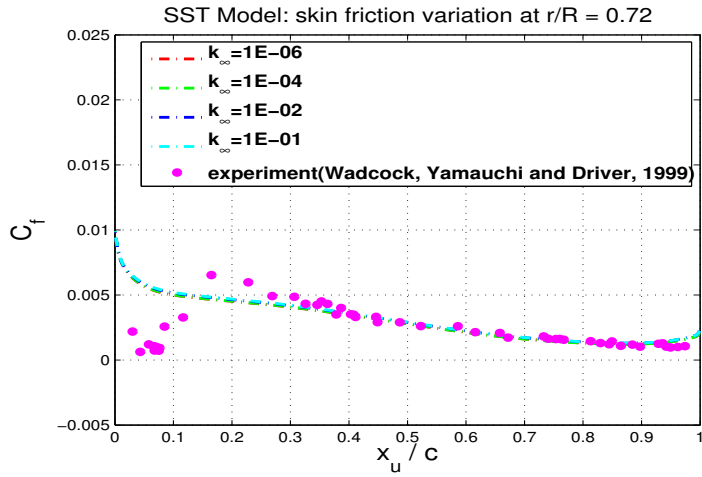


(e) $r/R = 0.50$

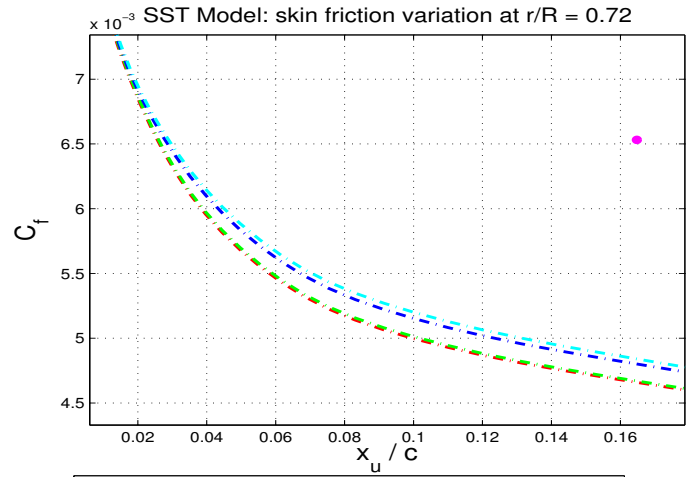


(f) enlarged view

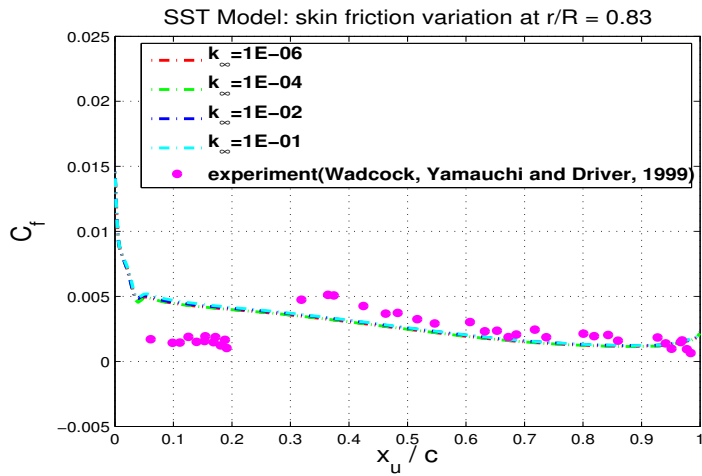
Figure 11: SST-DES Model: skin friction variation along x_u (upper surface of the blade) at various radial stations corresponding to 10-degree collective pitch



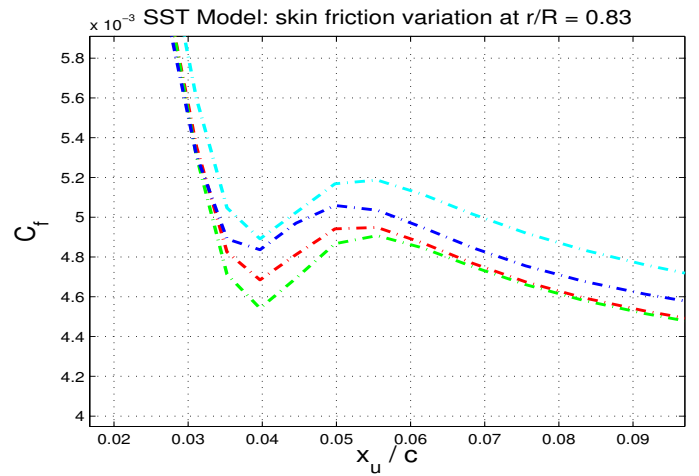
(a) $r/R = 0.72$



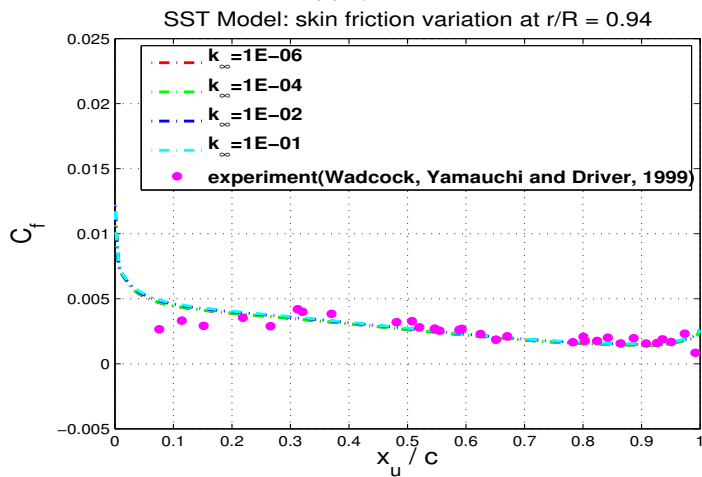
(b) enlarged view



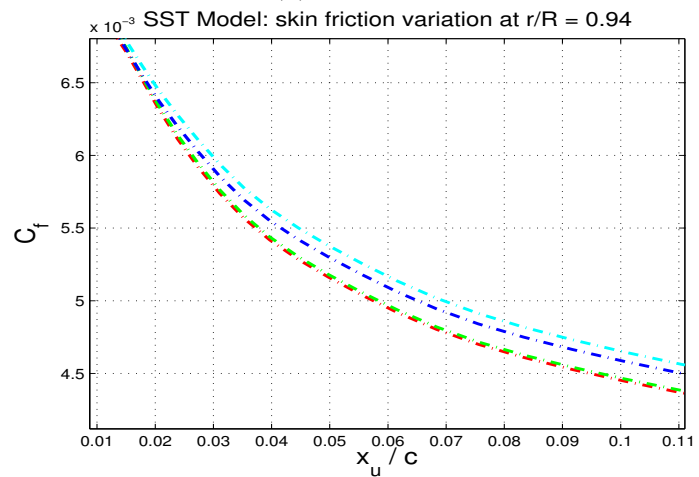
(c) $r/R = 0.83$



(d) enlarged view

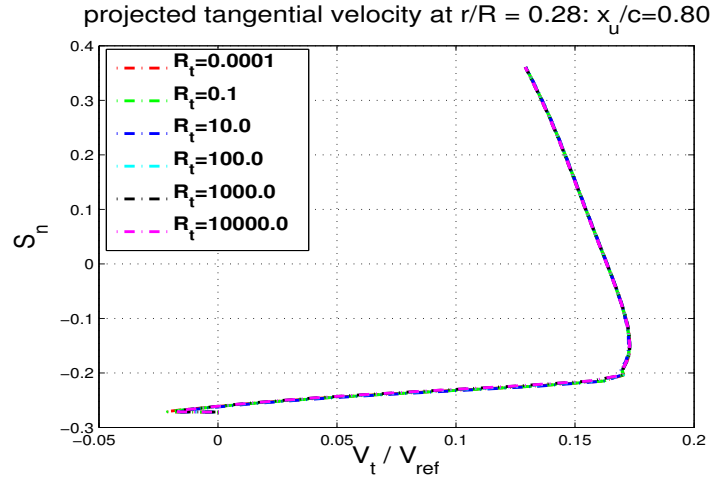


(e) $r/R = 0.94$

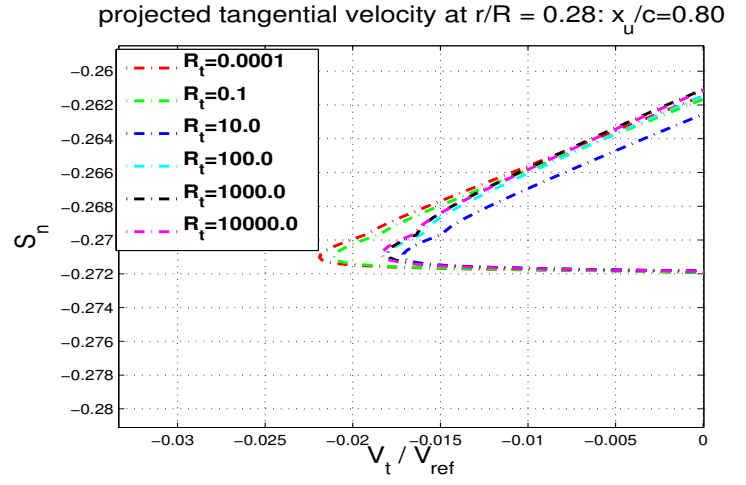


(f) enlarged view

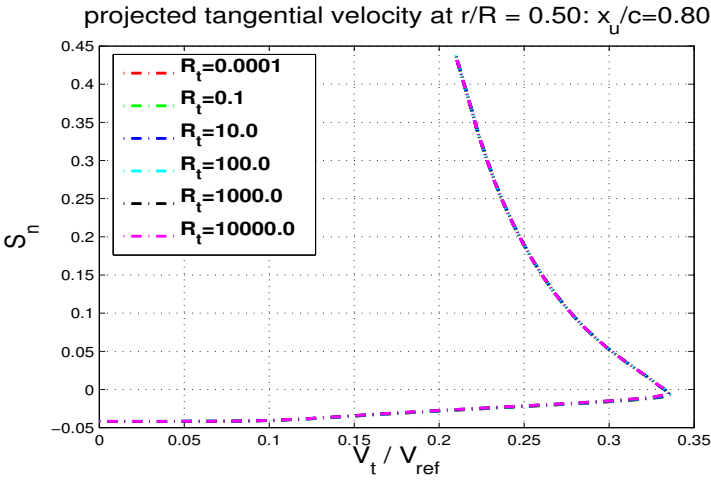
Figure 12: SST-DES Model: skin friction variation along x_u (upper surface of the blade) at various radial stations corresponding to 10-degree collective pitch



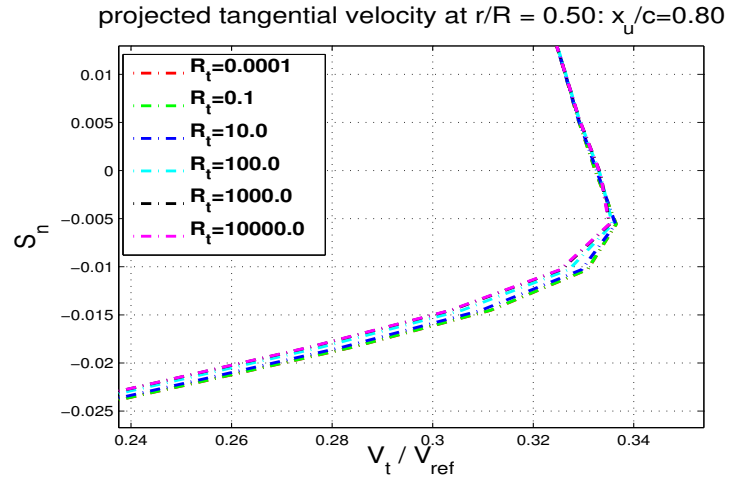
(a) $r/R = 0.28$



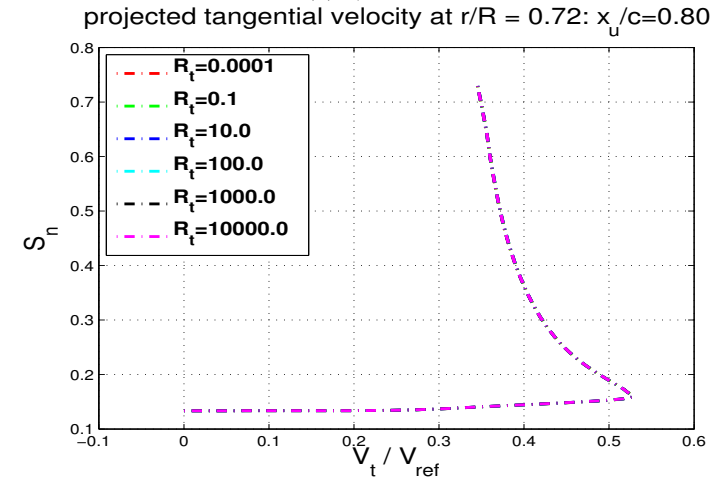
(b) enlarged view



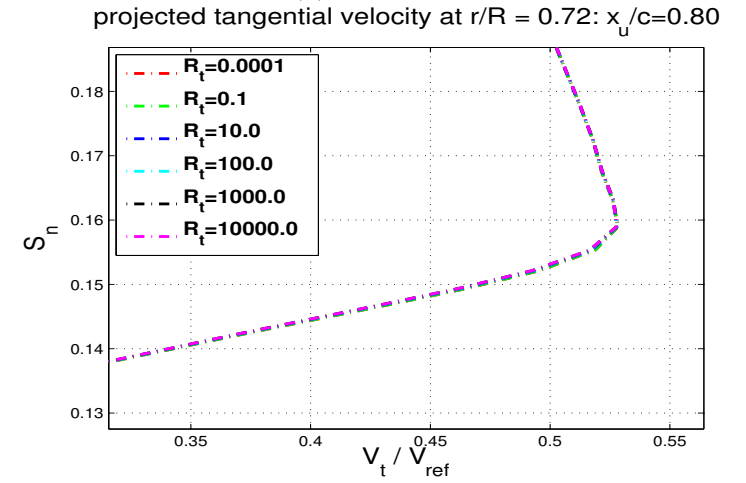
(c) $r/R = 0.50$



(d) enlarged view

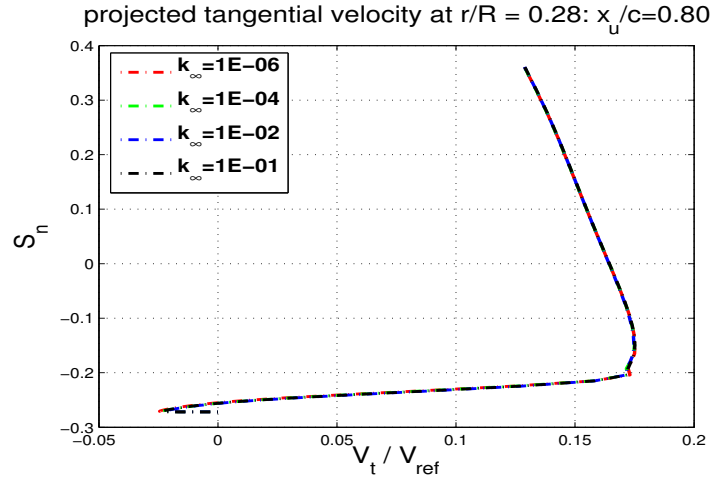


(e) $r/R = 0.72$

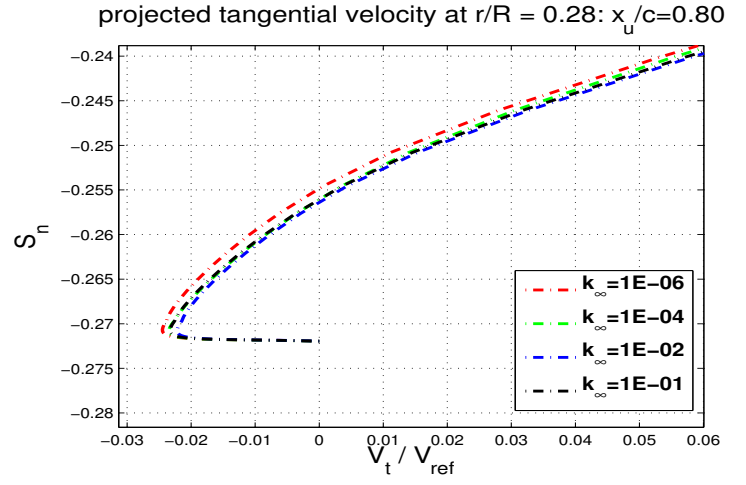


(f) enlarged view

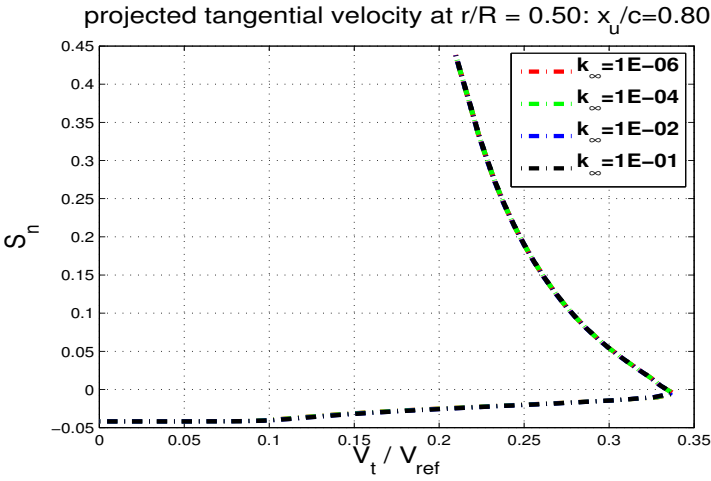
Figure 13: SA-DES Model: boundary layer profiles at $x_u/c=0.8$ corresponding to various radial stations



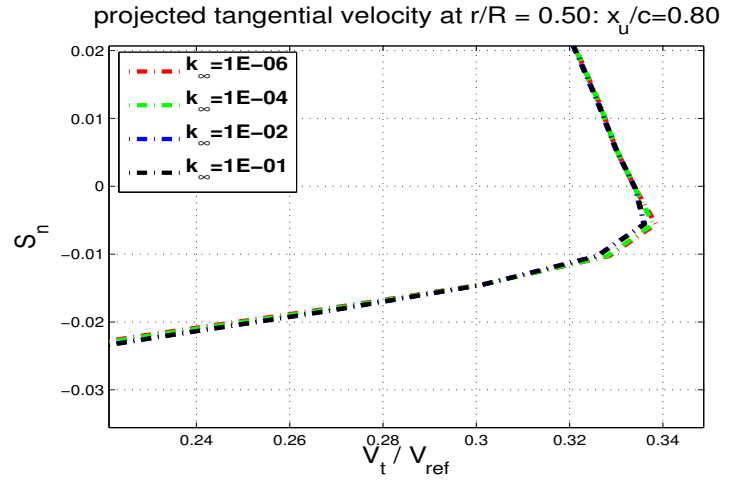
(a) $r/R = 0.28$



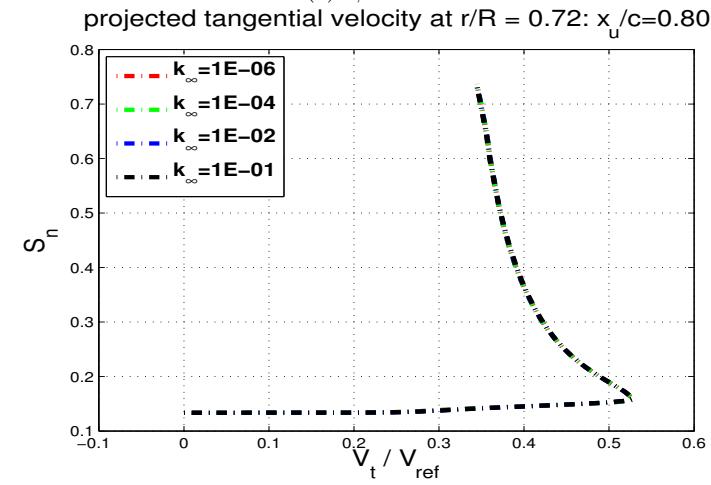
(b) enlarged view



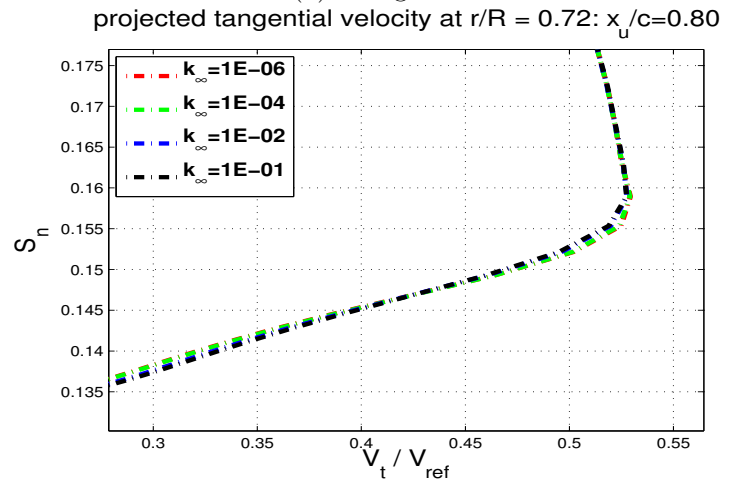
(c) $r/R = 0.50$



(d) enlarged view



(e) $r/R = 0.72$



(f) enlarged view

Figure 14: SST-DES Model: boundary layer profiles at $x_u/c=0.8$ corresponding to various radial stations